Numerical Study of Bluntness Impact on Performance of Integrated Dual-waverider without or with Duct

Chongguang Shi[1], Jan Martinez Schramm[2], Yiqing Li[3], Ralf Deiterding[4], Chengxiang Zhu[1] and Yancheng You[1]†

[1]School of Aerospace Engineering, Xiamen University, Xiamen, Fujian, 361005, China

[2]Spacecraft Department, Institute of Aerodynamics and Flow Technology, DLR German Aerospace Center, Göttingen, 37073, Germany

[3]School of Engineering, Nanchang Hangkong University, Nanchang, Jiangxi, 361005, China

[4]University of Southampton, Southampton, Britain

(Received xx; revised xx; accepted xx)

Method of curved shock-characteristic is developed based on the curved shock theory and applied to high-precision filowfield calculation in uniform/nonuniform, external/internal, planar/axisymmetry flow. The main idea is to solve the first-order gradients of pressure and flow deflection angle in the streamline-characteristic coordinate. With acquired derivatives, the aerodynamical parameters of post-shock flowfield can be evaluated. Compared with the method of characteristic, the iterative process of the method of curved shock-characteristic is simplified without sacrificing the accuracy by using gradients. Explicit equations are derived along the streamlines and characteristics. Several post-shock flowfields are solved using the method of curved shock-characteristic to validate the accuracy. The results show that the maximum differences are less than 0.5%. Besides, through gradients, it only takes a small number of mesh nodes for the method of curved shock-characteristic to calculate the flowfield under the condition that the accuracy doesn't decrease. The accuracy and simplicity make the method of curved shock-characteristic a good candidate for solving planar/axisymmetry flowfields and flow analysis.

Key words:

---

1. Introduction

In 1959, Nonweiler firstly derived a caret waverider from a notable inviscid two-dimensional flowfield F. (1959). With this design pattern, the waverider theory has been developed from generating two-dimension shock wave to axis-symmetry shock wave. In 1980, Rasmussen used the conical flowfield to design waverider based on the inviscid hypersonic small-disturbance theory Rasmussen & P. (1980). Since then, waveriders derived from conic flow have been studied extensively by many researchers.

However, when waveriders are generated from conic flow, the configuration geometry is limited by the standard flowfield. What's more, the shock wave generated by the traditional waverider is axis-symmetric, which restrains the application. Therefore, Sobieczky

† Email address for correspondence: yancheng.you@xmu.edu.cn

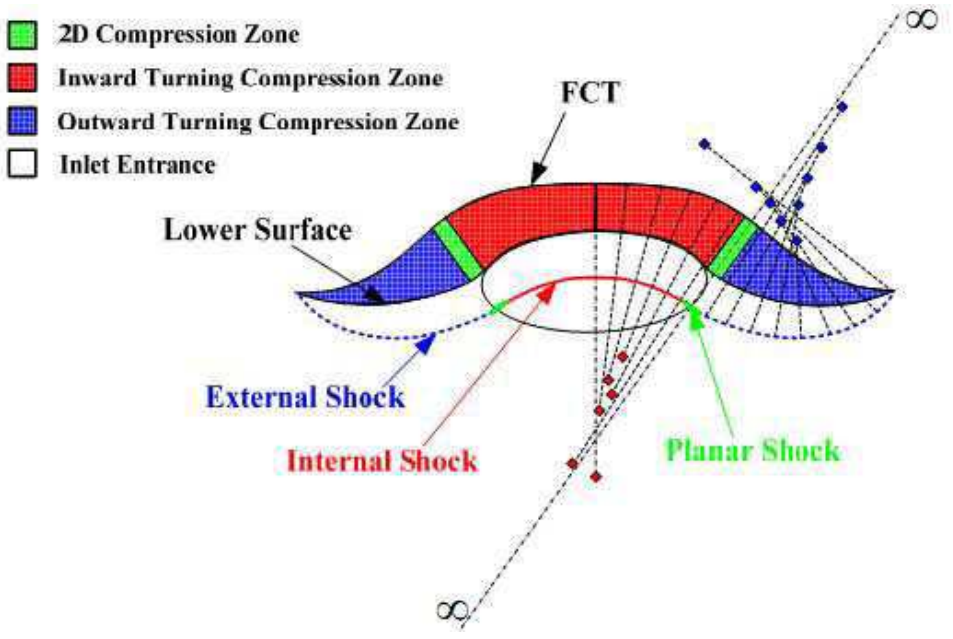

FIGURE 1. Sectional display of dual-waverider concept Y. *et al.* (2011)

presented the osculating-cone waverider theory to design waverider with generalized shock geometries in 1995 D. *et al.* (1995). The key idea was to decompose the three-dimensional flow to a series of two-dimensional or axis-symmetry flow in the osculation planes. Then the waverider is able to be generated with arbitrary shock geometries. With this theory, Takashima and Lewis illustrated a concept for the integration of a waverider and two-dimensional inlet N. & J. (1995). Nevertheless, all above theories are developed by considering the waverider as an external component. But for the internal flow and the external flow, the compression efficiencies are distinct C. (2011). To be specific, the compression efficiency for external flow is lower than that of internal flow. Thus, for the same shock wave angle, the deflection angle is smaller in the outward flowfield compared with inward flowfield, which leads to different compression surfaces. Therefore, waveriders generated from external and internal shock waves can't be connected directly.

2. Methodology

2.1. *Introduction of dual-waverider theory*

In 2011, the dual-waverider theory proposed a method to perfectly solve the transition problem Y. *et al.* (2011). A small piece of planar shock is introduced to transit the shock waves from external to internal smoothly, although their local curvature centers are in different sides of the shock, as shown in Fig.1.

In the figure, a three-dimensional shock wave composed of internal, planar and external shock waves is constructed based on the dual-waverider theory. Due to the planar shock, the local curvature radii of the external and internal shock waves are changed to infinity simultaneously in the transition place, which results in the same deflection angles. Thus, the dual-waverider is created as an overall design rather than a simple constitution of the two discrete components.

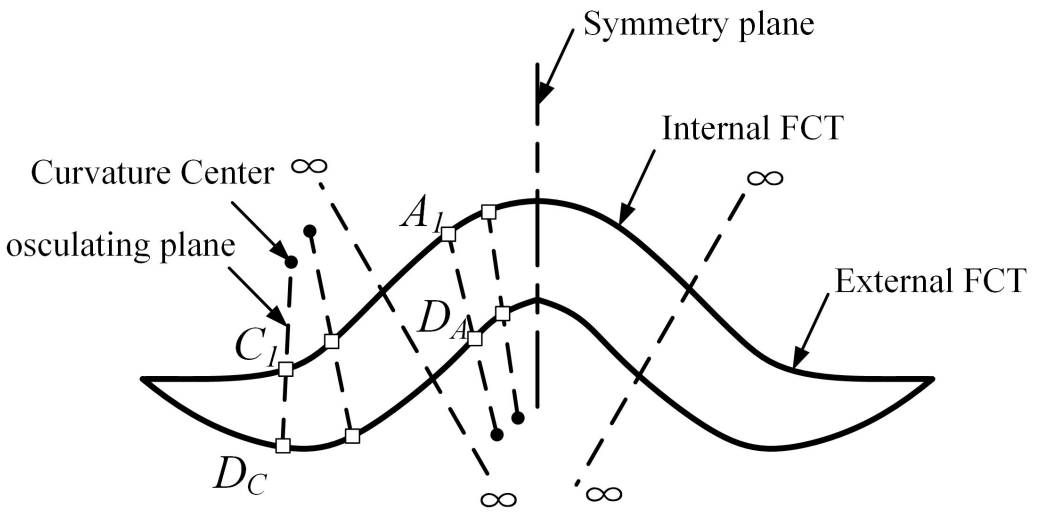

FIGURE 2. Flow capture tube in design plane

2.2. *Design of aerodynamic model with given pressure distribution*

In last section, the dual-waverider theory is illustrated. With this theory, a dual-waverider can be created with designed three-dimensional shock wave. However, shock waves are not parameters that can be related with the performance of the vehicle directly. That's why a design method of dual-waverider with given pressure distribution is necessary. The vehicle performance can be approximately calculated with given pressure distribution. Furthermore, there is lateral pressure gradient on the dual-waverider generated by given shock wave. But with a given pressure distribution, the lateral pressure gradient will disappear, which is beneficial to the vehicle performance. Based on this idea, a dual-waverider is created to combine the outward and inward flowfield according to the following steps. First, the flow capture tube (FCT) projected in the design plane is given. It consists of three parts which are internal FCT, planar point and external FCT, as shown in Fig.2. The curvature radii and centers of the FCT can be calculated by via the following equation

$$S = \frac{1}{R} = \frac{y''}{(1+y'^2)^{3/2}}, \tag{2.1}$$

and of course, the curvature radii of the planar point is infinity by design. The osculating plane is created by connecting the local curvature center and the corresponding point on the FCT. Since there is no lateral pressure gradient, the air flows in the osculating plane.

Then the FCT projected in the top view and the pressure distribution along the symmetry plan are given, as shown in the Fig.3. Owing to the stable lateral pressure, the pressure distribution of compression profiles is a part of the given pressure curve. For instance, A_1D_A is an internal compression profile. Based on the positions at the horizontal coordinate, the pressure curve AD is the design distribution along the internal compression profile A_1D_A. Similarly, the design pressure distribution along the external compression profile C_1D_C can also be intercepted from the given pressure curve along the symmetry plane. With the pressure distribution and oncoming flow parameters, compression profiles are solved in each osculating plane. Afterwards, the compression surface is constructed based on the compression curves and the included angle of the

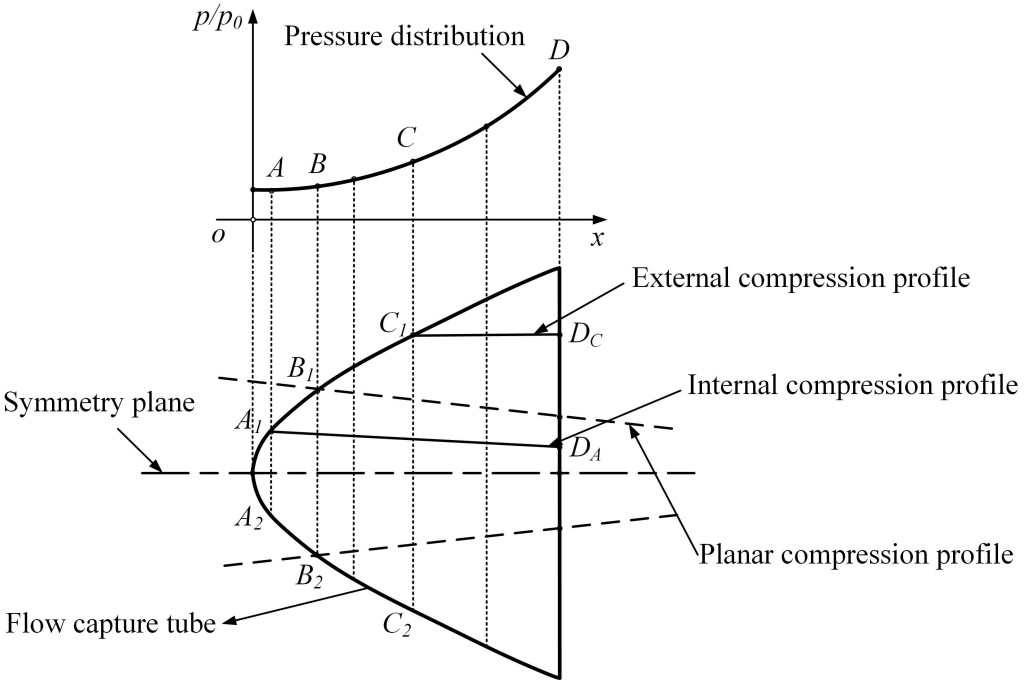

FIGURE 3. Schematic diagram of aerodynamic configuration with given pressure distribution

osculating plane and the symmetry plane. More specifically, the construction of the compression surface is realized by coordinate transformation. For example, after the external compression profile C_1D_C is solved, the projected coordinate values (x,y) are known along the curve C_1D_C. Assuming that the included angle of the local osculating plane and the symmetry plane is α, the three-dimensional coordinate values (x_{3D}, y_{3D}, z_{3D}) of the external compression profile C_1D_C can be calculated by $x_{3D} = x$, $y_{3D} = y \times \sin\alpha$ and $z_{3D} = y \times \cos\alpha$. The pattern is suitable for all the osculating plane. When the dual-waverider is acquired, it comes to the phase of the duct design. The geometry of the duct is set as a quasi-rectangular. The contour of the duct is stretched toward the oncoming flow and intersects with the three-dimensional shock wave. The intersecting curve is the three-dimensional shape of the duct cowl. Therefore, at the design Mach number, the incident shock wave will impinge the duct cowl and cause a reflected shock wave. Finally, in order to increase the volume, there is an integrated forebody in front of the dual-waverider. What's more, the three-dimensional shock wave structure is not changed by the forebody since there is no shock wave generated at the leading edge of the forebody. Shock waves occur at the joint of the forebody and dual-waverider due to the flow deflection. In a word, the study model is composed of three parts: the forebody, the dual-waverider and the duct. The forebody and dual-waverider are collectively called the integrated dual-waverider.

The integrated dual-waverider with duct is shown in Fig.4. The design Mach number is 7 and the original length is 0.742 m. The prototype is blunted with a radius of 0.3mm and 0.5mm to investigate the bluntness impact on performance of integrated dual-waverider without/with duct. CAD software is applied to deal with the surface manipulation and blunting process.

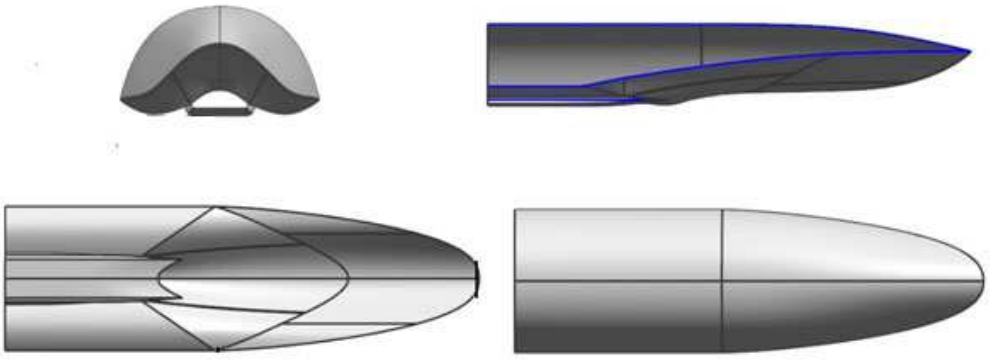

FIGURE 4. Geometry of integrated dual-waverider with duct

3. **CFD numerical method**

This section elaborates the governing equations and numerical method used in this work and a double ellipsoid case is presented to validate the numerical method.

3.1. *Computational Model*

The governing equations for Steady-State full Navier-Stokes equations are W. (2014)

Continuity equation:

$$\frac{\partial \rho}{\partial t} + \frac{\partial \rho u}{\partial x} + \frac{\partial \rho v}{\partial y} + \frac{\partial \rho w}{\partial z} = 0, \tag{3.2}$$

X-momentum equation:

$$\frac{\partial \rho u}{\partial t} + \frac{(\partial \rho u^2 + \sigma_x)}{\partial x} + \frac{(\partial \rho uv + \tau_{xy})}{\partial y} + \frac{(\partial \rho uw + \tau_{xz})}{\partial z} = 0, \tag{3.3}$$

Y-momentum equation:

$$\frac{\partial \rho v}{\partial t} + \frac{(\partial \rho vu + \tau_{yx})}{\partial x} + \frac{(\partial \rho v^2 + \sigma_y)}{\partial y} + \frac{(\partial \rho vw + \tau_{yz})}{\partial z} = 0, \tag{3.4}$$

Z-momentum equation:

$$\frac{\partial \rho w}{\partial t} + \frac{(\partial \rho wu + \tau_{zx})}{\partial x} + \frac{(\partial \rho wv + \tau_{zy})}{\partial y} + \frac{(\partial \rho w^2 + \sigma_z)}{\partial z} = 0, \tag{3.5}$$

Energy equation:

$$\begin{aligned} \frac{\partial e}{\partial t} &+ \frac{[(e+\sigma_x)u + v\tau_{yx} + w\tau_{zx} - k\frac{\partial T}{\partial x}]}{\partial x} \\ &+ \frac{[(e+\sigma_y)v + u\tau_{xy} + w\tau_{zy} - k\frac{\partial T}{\partial y}]}{\partial y} \\ &+ \frac{[(e+\sigma_z)v + u\tau_{xz} + v\tau_{yz} - k\frac{\partial T}{\partial z}]}{\partial z} = 0. \end{aligned} \tag{3.6}$$

Parameter	Pressure case	Heat flux case
Mach number	8.02	8.04
Stagnation pressure (MPa)	8.5	7.8
Stagnation temperature (K)	720	892
Re (m^{-1})	1.98×10^7	1.13×10^7

TABLE 1. Freestream flow conditions of double ellipsoid.

where,

$$p = p(\rho, \xi), \xi = \frac{e}{\rho} - \frac{u^2+v^2+w^2}{2}, \sigma_x = p - \lambda(\frac{\partial u}{\partial x} + \frac{\partial v}{\partial y} + \frac{\partial w}{\partial z}) - 2\mu\frac{\partial u}{\partial x}$$

$$\sigma_y = p - \lambda(\frac{\partial u}{\partial x} + \frac{\partial v}{\partial y} + \frac{\partial w}{\partial z}) - 2\mu\frac{\partial v}{\partial y}, \sigma_z = p - \lambda(\frac{\partial u}{\partial x} + \frac{\partial v}{\partial y} + \frac{\partial w}{\partial z}) - 2\mu\frac{\partial w}{\partial z}$$

$$\tau_{xy} = \tau_{yx} = -\mu(\frac{\partial u}{\partial y} + \frac{\partial v}{\partial x}), \tau_{xz} = \tau_{zx} = -\mu(\frac{\partial u}{\partial z} + \frac{\partial w}{\partial x}), \tau_{yz} = \tau_{zy} = -\mu(\frac{\partial v}{\partial z} + \frac{\partial w}{\partial y})$$

The governing equations are discretized and numerically integrated based on a finite-volume approach. The turbulence model version is k-w SST. Inviscid flux is solved using upwind difference based on AUSMDV which is also recognized as the Improved Advection Upwind Splitting Method. It is a blend of AUSMD and AUSMV, where "D" and "V" denote a flux-Difference- splitting-biased scheme and flux-Vector-splitting-biased one, respectively Y. & S. (1994). Higher order accuracy is acquired with MUSCL and a limiter. Central difference scheme and euler backward difference method with fully implicit scheme are used to calculate viscous flux and temporal integration respectively.

In this research, a calorically perfect gas model is assumed, and the Sutherland's law is applied to evaluate the viscosity as follow,

$$\mu = \mu_0(\frac{T}{T_0})^{\frac{3}{2}}(\frac{T_0+S}{T+S}). \tag{3.7}$$

where the symbols, μ_0 and T_0, represent the freestream parameters with the values $\mu_0 = 1.716 \times 10^{-5} kg/m \cdot s$, $T_0 = 273.11K$, and $S = 110.56K$.

Equations (3.2-3.7) form a closed system of partial differential equations, which must be solved with a suitable set of initial and boundary conditions. Inflow boundary conditions are fixed with values of oncoming flow parameters, and outflow boundary conditions are set to pressure outlet. Wall boundary conditions include a non-slip condition and an isothermal condition for temperature.

3.2. *Numerical test case*

In this research, heat flux and lift-drag ratio are evaluated under different blunt radii. Therefore, a test model with heat flux and pressure experiment data is chosen from the reference X. (2007). The test model is a double ellipsoid shown in Fig.5 and the detailed size could be found in the reference X. (2007). The three-dimensional hypersonic viscous flowfield around the double ellipsoid is simulated and analyzed. Flow parameters are as follows:

Figure 6 is the grid structure used in this case. The double ellipsoid is simulated with minimum near-wall grid spacing of 1×10^{-6} m and the wall normal expansion ratio is 1.1.

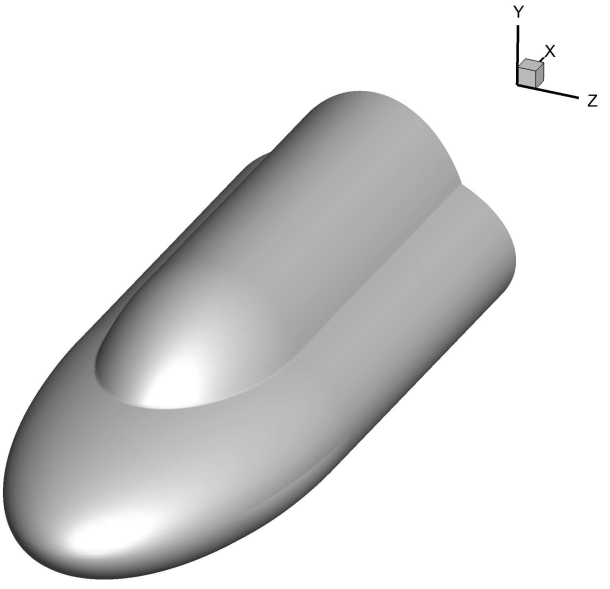

FIGURE 5. Geometry of double ellipsoid

The number of total cells is 7.7 million and the yplus is less than 1. In this case, the heat flux is normalized by the heat flux of the leading-edge stagnation point of a standard sphere q_{ref} and presented in terms of the dimensionless parameter $\frac{q}{q_{ref}}$, the pressure is presented in terms of the dimensionless parameter $\frac{P}{P_{t2}}$ normalized by the pressure of the leading-edge stagnation point of the double ellipsoid, P_{t2}. Fig.7 and Fig.8 show the results.

Figure 7 shows the experimental and computational dimensionless pressure distribution of the symmetry plane with black curve and red curve respectively. The pressure of the leading-edge stagnation point of the double ellipsoid, P_{t2}, is equal to 69.024kpa. From the picture, the pressure decreases continually until the flow impinges the second ellipsoid, which causes a sharp rise of pressure. Then the pressure declines again due to the geometry of the upper surface. The pressure distribution, predicted with the numerical method, are almost consistent with the experimental results, which demonstrates the capability of this numerical method to precisely calculate the pressure distribution. As for the heat flux shown in Fig.8, the black curve stands for the experimental values while the computational results are presented with red line. The heat flux of the leading-edge stagnation point of a standard sphere q_{ref} is $568.4kw/m^2$. Same as the pressure distribution, the heat flux goes down at the beginning and then surges to a peak owing to the impingement. Although there are deviations between the experimental and computational results, the tendency of the simulation curve is coincident with the experimental one.

Therefore, the numerical method is capable of predicting heat flux and pressure distribution. However, one point is needed to declare that values of dimensionless heat flux, predicted by this numerical method, are a little bigger than experimental values in some sections. It should be due to the turbulence model and some relevant work will be carried out in the future research.

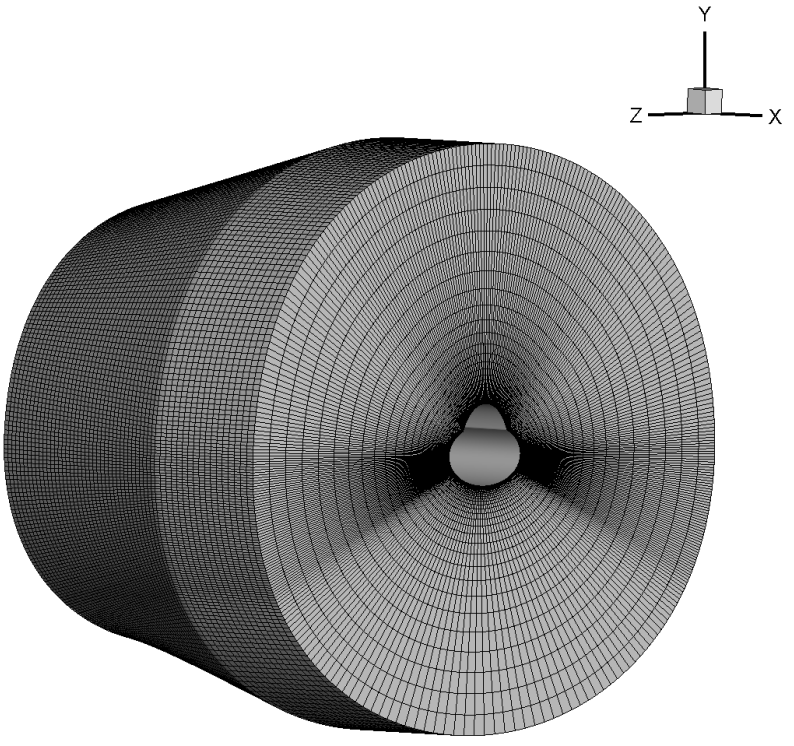

FIGURE 6. Mesh of double ellipsoid

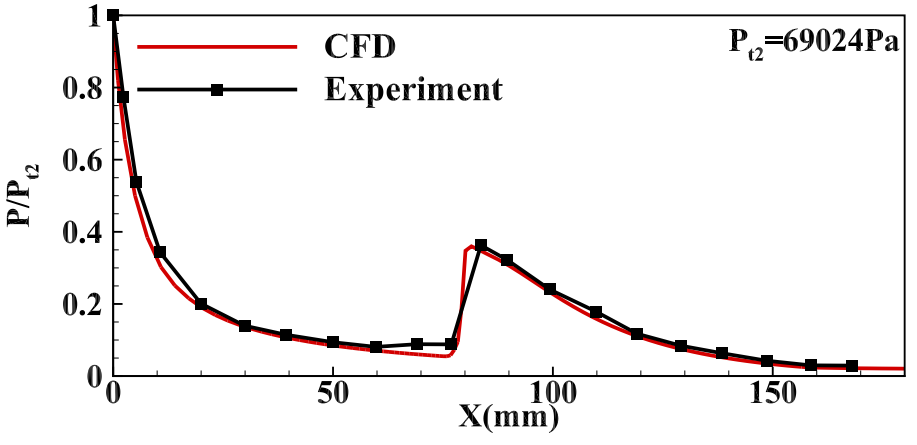

FIGURE 7. Numerical and experimental pressure along centerline of double ellipsoid

3.3. *Freestream conditions and mesh*

The research case is an integrated dual-waverider model without/with duct. The results exhibited here are under the conditions of Ma = 7.4 without angle of attack. Parameters of the oncoming flow are listed in Table 2. The grid structure is shown Fig.9. With $y^+ < 1$ and approximate 41 million cells for half model, the grid resolution is sufficient to acquire

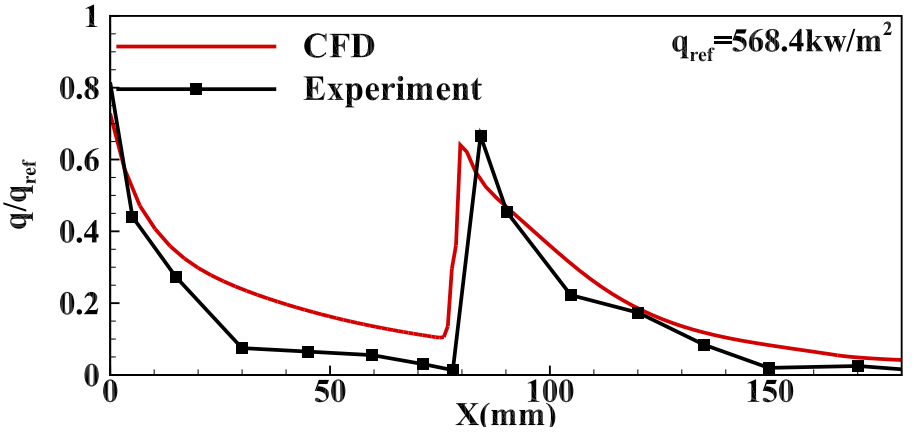

FIGURE 8. Numerical and experimental heat flux along centerline of double ellipsoid

Parameter	Value
Mach number	7.4
Static pressure (Pa)	1990
Static temperature (K)	226
Density (kg/m^3)	0.0259
Velocity (m/s)	2410

TABLE 2. Freestream flow conditions of dual-waverider.

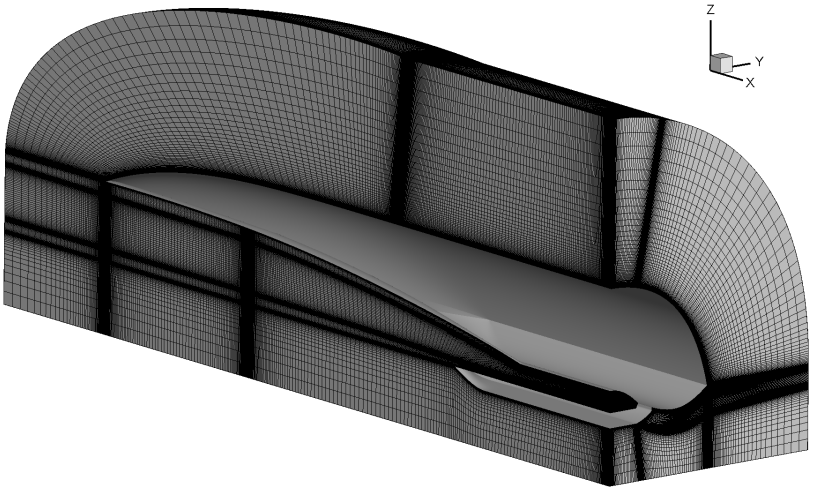

FIGURE 9. Mesh of dual-waverider with duct

grid-converged results. Inflow boundary conditions are set with values of freestream parameters, and outflow boundary conditions are set to pressure outlet. Wall boundary conditions contain a non-slip condition and an isothermal condition for temperature. The wall temperature is chosen as T_w=300K.

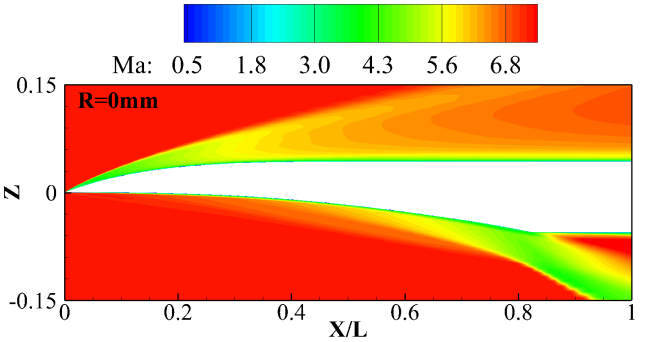

(a) Mach number contour of the symmetry plane without bluntness

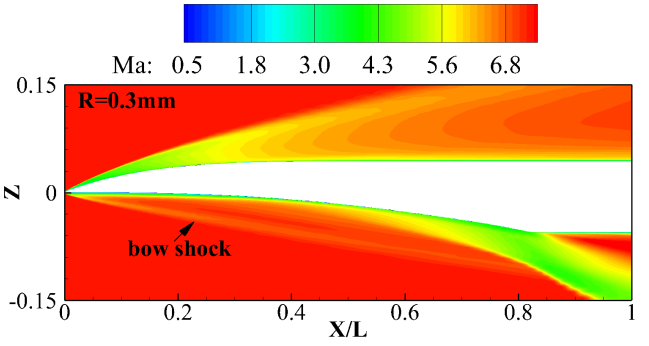

(b) Mach number contour of the symmetry plane with blunt radius of 0.3mm

FIGURE 10. Mach number contour of the symmetry plane with different blunt radii

4. Performance analysis of bluntness

This section analyzes the bluntness impact on aerodynamic performance as well as heat flux of dual-waverider.

4.1. *Aerodynamic coefficient*

The aerodynamic performance of the integrated dual-waverider without duct is firstly studied at the different radii. Fig.10 shows the Mach number contours at the symmetry plane of the original integrated dual-waverider and the integrated dual-waverider with 0.3mm leading edge. The shock wave attaches to the leading edge of the original integrated dual-waverider whereas a bow shock which increases the wave drag is observed when the leading edge is blunted.

The differences of flowfield structure causing by the bluntness lead to the changes of the aerodynamic coefficients. Table 3 presents the aerodynamic coefficients of the integrated dual-waverider with different leading-edge radii. C_{D-p}, C_{D-v} and C_D represent the pressure component of drag coefficient, the viscosity component of drag coefficient and the total drag coefficient blunted with different radii respectively. C_L and C_D/C_L stand for the lift coefficient and the lift-drag ratio of the integrated dual-waverider respectively. From the table, it is known that with the increase of the bluntness, the pressure component rises at the beginning and then declines whereas the viscosity component goes down continually. However, since the pressure component is about twice as large as the viscosity component, the total drag coefficient has the same tendency with the pressure component. But owing to the influence of viscosity, although the pressure component at

Without duct	C_{D-p}	C_{D-v}	C_D	C_L	C_D/C_L
R = 0mm	0.01364	0.00712	0.02077	0.01344	0.6471
R = 0.3mm	0.01353	0.00677	0.02030	0.01297	0.6389
R = 0.5mm	0.01371	0.00668	0.02039	0.01288	0.6317

TABLE 3. Aerodynamic coefficients at different blunt radii.

the bluntness radius of 0.5mm is bigger than the sharp one, the total drag coefficient of the integrated dual-waverider with 0.5mm leading edge is less than the prototype.

For a direct understanding of the force variation, Fig.11 shows aerodynamic coefficients of dual-waverider with different blunt radii. Same as above, C_D (red curve), C_L (black curve) and C_D/C_L (blue curve) denote the total drag coefficient, the lift coefficient and the lift-drag ratio that the prototype configuration generates for different leading edges. From the figure, it is shown that both the drag and lift decrease when the leading edge increases to 0.3mm. Although, the bow shock generated by the bluntness has a positive effect on the drag, the leakage of high-pressure flow is the major reason for the force degradation. As for the original configuration, the shock wave is attached on the vehicle body and the flow doesn't circulate between the upper and lower surfaces. However, when the leading edge is blunted, the upper and lower regions are connected and the flow runs from the high-pressure area to the low-pressure area owing the pressure difference. To be specific, the flow seeps from the lower surface into the upper surface of the forebody whereas the flow in the upper region permeates the lower region. The flow leaks around the leading edges lead to a decrease of 3.5% and 2.3% on the lift and drag coefficients respectively. When the bluntness radius rises from 0.3mm to 0.5mm, the bow shock becomes stronger, which brings an increase of the pressure distribution. Owing to the pressure variation, the leakage declines around the forebody and improves around the dual-waverider. That's why the lift goes down continually with a value 0.7% but the drag increases 0.4% when the bluntness changes from 0.3mm to 0.5mm. With combined effects of the drag and lift coefficients, the lift-drag ratio declines continually with a value 1.3% and 1.1% for 0.3mm and 0.5mm leading edges separately. Furthermore, the lift-drag ratio maintains at a low level for various leading edges due to the forebody. Since the forebody is designed to increase the volume of the configuration and not to destroy the shock wave structure generated by the dual-waverider, there is no shock in front of the lower surface of the forebody whereas a shock stands in front of the upper surface of the forebody. Without the pressure jump caused by a shock wave, the forebody generates negative effects on the lift, which makes the lift-drag ratio of this configuration lower than 1.

In terms of the integrated dual-waverider with duct, the Mach number contours at the symmetry plane of the original and blunted integrated dual-waverider with duct are presented in Fig.12. Similar to the configuration without duct, there is an attached shock wave at the leading edge of the original integrated dual-waverider whereas a bow shock in front of the blunted leading edge. Then a second incident shock wave is generated at the joint of the forebody and dual-waverider leading to a pressure increase. Compared the flowfields of the configuration without or with duct, it is clear that since the upstream parameters decide the pattern of downstream flowfield in supersonic flow, flow structures before the duct are the same for the configuration without or with duct. However, in the region of duct, the differences occur. Unlike the configuration without duct, the pressure inside the duct increases continually because of the shock wave reflection. What's more,

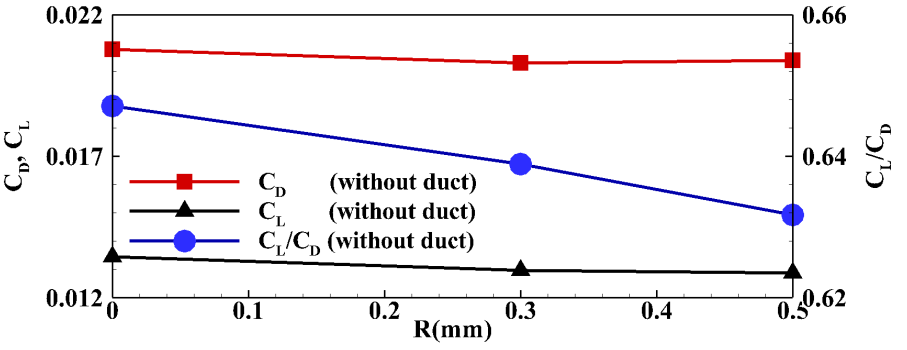

FIGURE 11. Aerodynamic coefficients of dual-waverider with different blunt radii

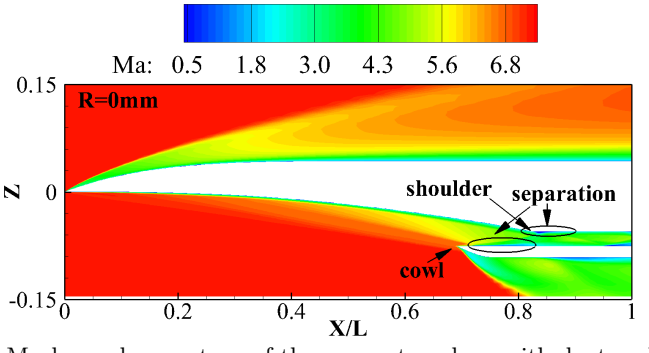

(a) Mach number contour of the symmetry plane with duct and sharp leading edge

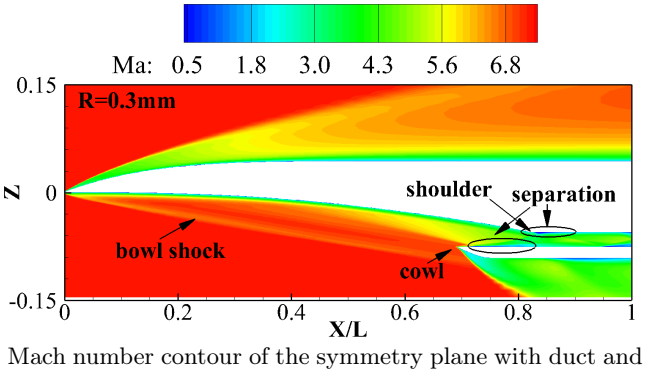

(b) Mach number contour of the symmetry plane with duct and 0.3mm leading edge

FIGURE 12. Mach number contour of the symmetry plane with duct at different blunt radii

there is a tiny separation at the cowl and shoulder of the duct due to the interaction of the reflected shock wave and boundary layer.

Aerodynamic coefficients of the integrated dual-waverider with duct at different leading edges are shown in Fig.13. In the picture, the red curve, black curve and blue curve stand for the total drag coefficient C_D, the lift coefficient C_L and the lift-drag ratio C_D/C_L respectively. From the figure, it is clear that the force coefficients of the configuration with duct have an opposite trend compared with force coefficients of the configuration without duct. What's more, with the added duct, the drag coefficient becomes larger

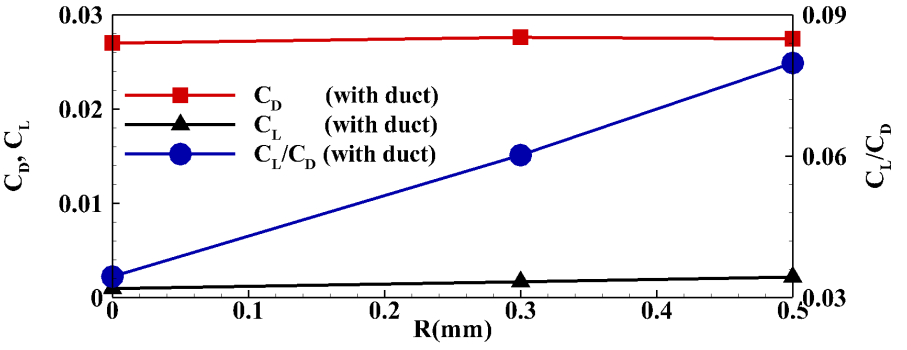

FIGURE 13. Aerodynamic coefficients vs. different blunt radii of dual-waverider with duct

and the lift coefficient is lower. Therefore, the duct is regarded as a drag component rather than a lift component for the vehicle. Fig.14 shows the pressure distribution along the centerline of the original configuration with duct. The upper and lower surfaces of the shock wave generator (SWG) are presented with black and red curves respectively. As for the duct, blue curves stand for the upper surface while green curves represent the lower surface. Since the lift is created by the pressure difference of the upper and lower surfaces, the forebody where the upper surface pressure is bigger than that of the lower surface generates negative lift forces. Similarly, from the pressure distribution of the upper and lower surfaces of the duct, it is obvious that the duct brings negative effects on the lift. Furthermore, the windward area that positively correlates with the drag increases owing to the duct. Therefore, with the duct, the drag increases significantly. When the leading edge is blunted, the leakage of high-pressure flow still exists and a bow shock which increases the shock wave drag comes out. However, unlike the case of the configuration without duct, the parameters variation of the duct is the major factor of the force differences. As the bluntness rises, the pressure of the lower surface of SWG increases due to the changed shock structure. On the contrary, the pressure of the upper duct declines. Under the effect of pressure variation, the lift goes up continually when the leading edge is blunter. Besides, owing to the changed shock structure, the separation at the cowl and shoulder of the duct becomes larger as the bluntness increases, which results in a rise of the viscous part of drag. Different from the configuration without duct, the lift-drag ratio has positive relation with the leading edge radius. However, because of the forebody and duct, the lift-drag ratio of the configuration with duct is much smaller than that of the configuration without duct.

4.2. *Heat flux*

Figure 15 shows the variation trend of the heat flux along the upper surface centerline with different blunt radii. Red curves denote the heat flux of the original configuration while black and blue curves stand for the heat flux at the 0.3mm and 0.5mm leading edge respectively. Solid and dashed curves are used to divided the prototype without or with a duct. The horizontal coordinate is normalized with the length of the vehicle, L, and the vertical coordinate is the Stanton number (S_t) which illustrates the heat transfer between the flow and wall. The dimensionless number, S_t, can be calculated as follow,

$$S_t = \frac{h}{\rho u c_p}. \tag{4.8}$$

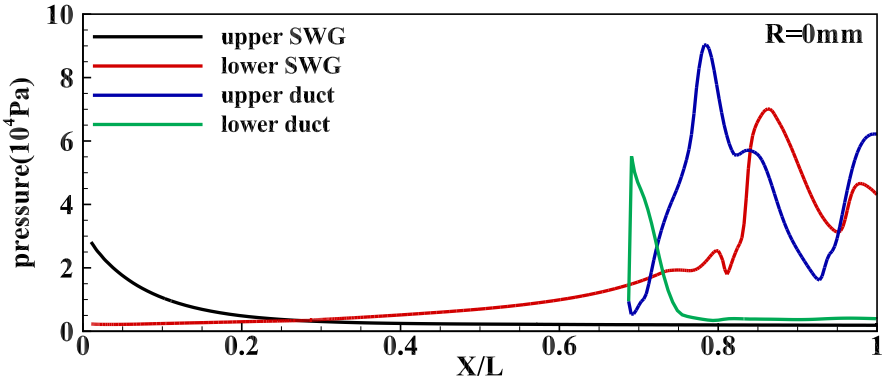

FIGURE 14. Pressure distribution along the centerline of the original configuration with duct

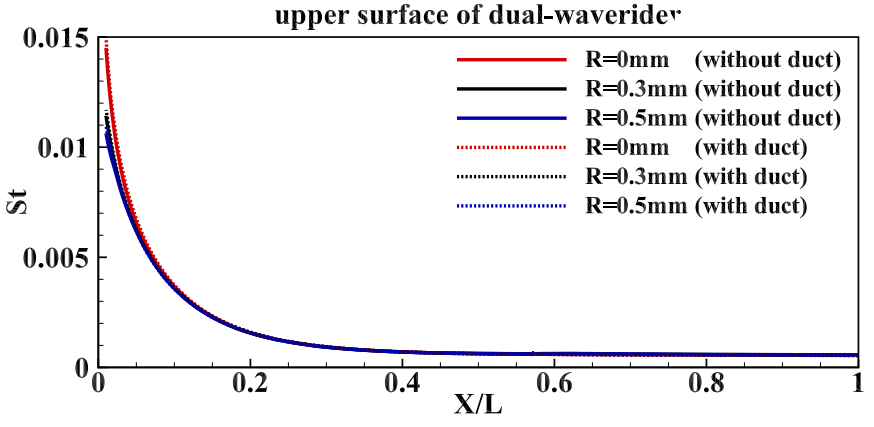

FIGURE 15. Heat flux along the upper surface centerline at different blunt radii

where the symbols, ρ, u and c_p, represent the density, velocity and specific heat capacity of the flow. For different leading edges, the heat flux distributions are similar because the geometry of the upper surface is almost the same. The heat flux reduces gradually at the beginning owing to the flow expansion and remains stable after $X/L = 0.4$ because the flow doesn't deflect. However, due to the change of leading edge, the maximum values of the heat flux are different and have a negative correlation with the leading edge bluntness. In other words, the bluntness is able to reduce the heat flux at the leading edge, which is beneficial to the thermal protection. The pattern is irrelevant to the duct because the upper surface geometry doesn't change with a duct installed.

Due to the different flow pattern, the variation trend of heat flux on the low surface of SWG is different from that on the upper surface. Shown in the Fig.16, the heat flux keeps rising before $X/L = 0.8$ at where the inlet shoulder is located. Before the shoulder, the flow is compressed gradually which increases the heat transfer between the flow and wall. With the compressive strength rises along the surface, the heat transfer rate also increases. When the flow passes the shoulder, there is an expansion region which leads to a significant reduce of heat flux. For the configuration without duct, the heat flux declines continually until the end. However, as for the configuration with duct, heat flux goes up again after the shoulder because of the reflection shock wave. What's more, a separation

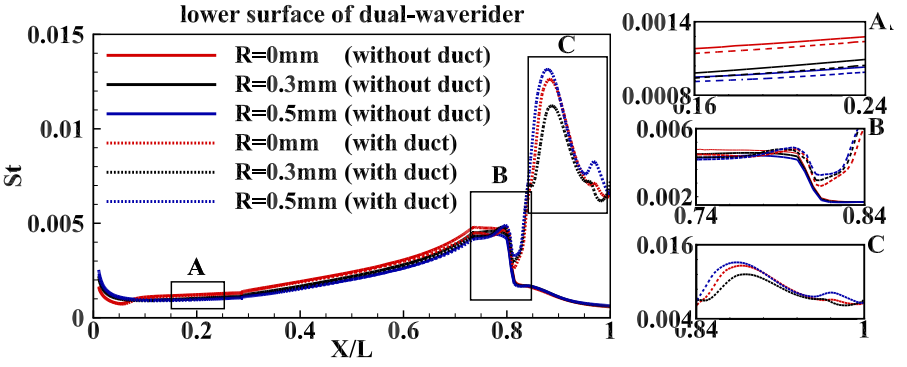

FIGURE 16. Heat flux along the lower surface centerline at different blunt radii

comes out due to the interaction of the reflection shock wave and the boundary layer at the shoulder. Therefore, in the separation region, the heat flux keeps rising and researches a peak at the end of the separation. Then it declines gradually until the end of the lower surface of SWG. In terms of the bluntness impact on the heat flux, before the shoulder ($X/L = 0.8$), the pattern is the same for the configuration without or with duct, because in supersonic flows, the changes of downstream flow don't affect the upstream flowfields. From the zoom area A, it is obvious that bluntness has a positive impact on the heat flux degradation. In zoom region B where the shoulder is located, the solid curves of three colours almost coincide. Therefore, after the expansion, the heat flux of the vehicle without duct at various radii decreases to the same level. Nevertheless, in the cases of the configuration with duct, the blunter leading edge leads to a higher heat transfer due to the changed strength of the reflection shock wave. Furthermore, the separation caused by the interaction of shock wave and boundary layer has a positive association with the bluntness. Thus, shown in the zoom region C, the heat flux of the configuration at 0.5mm leading edge is the maximum. In a word, the bluntness of the leading edge has opposite effects on the heat transfer of the configuration with duct before and after the reflection shock wave.

The heat flux distributions on the upper surface of the duct at different radii are presented in Fig.17. Same as above, the horizontal and vertical coordinates are set with dimensionless variables, X/L and S_t. The duct range is from $X/L = 0.69$ to $X/L = 1$. The red, black and blue dashed curves stand for different leading edge radii. The trends of heat flux for different leading edges are similar. Since the duct is designed with a sharp leading edge, the heat flux is extremely high at the cowl. Then it crashes to a low level until the incident shock wave impinges on the upper surface of the duct. When the shock wave interacts with the boundary layer, a separation is created. Under effects of the interaction, the heat flux increases gradually to a peak with the value around $S_t = 0.2$ and then declines due to the disappearance of the separation. The heat flux rises again at the region around $X/L = 0.93$ because the shock wave reflects in the duct and impinges on the upper surface of the duct again. Although the overall trends are similar, there are still some differences between various configurations. To be specific, a bow shock is generated because of the bluntness and the flow parameters before the incident shock wave are different. Therefore, the reflected shock angles are various at different leading edges and so are sizes of the separation. Due to this factor, the first maximum heat flux on the duct of the original configuration is higher but occurs later than the other two configurations. As the bluntness increases, the position of the maximum heat flux

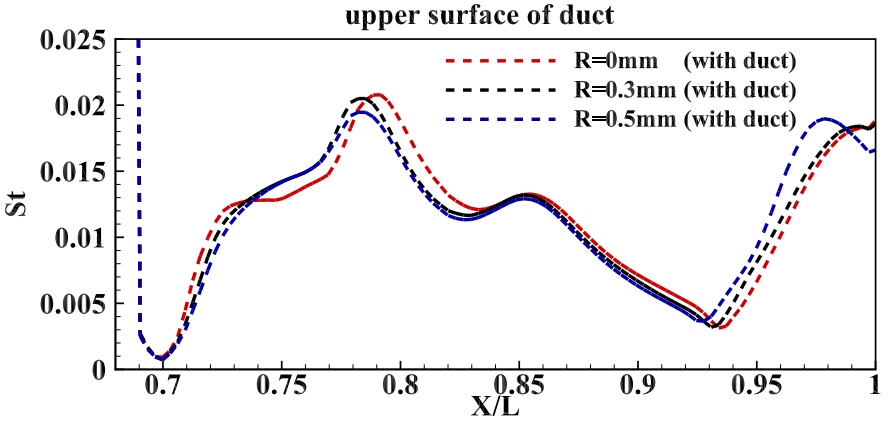

FIGURE 17. Heat flux along the upper surface centerline of the duct at different blunt radii

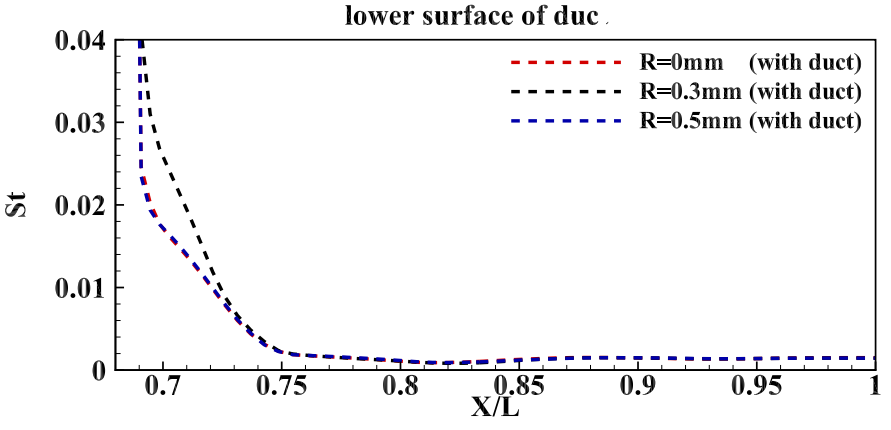

FIGURE 18. Heat flux along the lower surface centerline of the duct at different blunt radii

moves upstream and the maximum value declines. For the second maximum heat flux, the pattern should be the same. However, the duct is not long enough to show the pattern.

In terms of the lower surface of the duct, the heat flux distributions along the centerline are shown in Fig.18. The variables for the horizontal and vertical coordinates are the same as above. Since there is an expansion area at the place from $X/L = 0.69$ to $X/L = 0.75$, the heat flux declines continually in this region. Then it remains stable until a separation arises. Owing to the separation, the heat flux rises slightly in the separation region. From the comparison, the bluntness impact on the heat flux of the lower surface of the duct is limited and similar to the upper surface of the configuration.

5. Conclusions

This chapter studies the bluntness impact on the force and heat flux performance of the integrated dual-waverider without and with duct. When the leading edge of the configuration is sharp, the shock wave attached to the vehicle prevents the high-pressure flow penetrating the low-pressure regions. As the bluntness of the leading edge increases, the flow leaks from high-pressure regions into the low-pressure areas, which leads to a decrease of the lift for the configuration without duct. Nevertheless, with the duct

installed, the pressure variation on the surfaces of the duct has a stronger effect on the lift. When the leading edge is blunter, the lift is larger for the configuration with duct. The variation trends of the drag and lift-drag ratio are also distinct for the configuration without/with duct. The lift-drag ratio decreases when the leading edge radius increases for the configuration without duct whereas the lift-drag ratio of the vehicle with duct has a positive correlation with the bluntness. As for heat flux, the maximum value can be reduced effectively by blunting the leading edge. Nevertheless, the influence is weaker when the leading edge radius rises. The bluntness not only affects the heat flux on the nose region but also has an effect on the lower surface of the configuration and the upper surface of the duct by changing the shock structures.

Acknowledgements

We would like to acknowledge the support of the National Natural Science Foundation of China (NSFC, grant no.91941103) and Aeronautical Science Foundation of China (ASFC, grant no.2018ZB68008).

Declaration of Interests

The authors report no conflict of interest.

REFERENCES

C., You Y. 2011 An overview of the advantages and concerns of hypersonic inward turning inlets. *Aiaa International Space Planes & Hypersonic Systems & Technologies Conference* .

D., Jones K., H., Sobieczky, R., Seebass A. & C., Dougherty F. 1995 Waverider design for generalized shock geometries. *Journal of Spacecraft and Rockets* **32** (6), 957–963.

F., Nonweiler T. R. 1959 Aerodynamic problems of manned space vehicles. *The Aeronautical Journal* **63** (585), 521–528.

N., Takashima & J., Lewis M. 1995 Wedge-cone waverider configuration for engine-airframe interaction. *Journal of Aircraft* **32** (5), 1142–1144.

Rasmussen & P., Ford M. 1980 Waverider configurations derived from inclined circular and elliptic cones. *Journal of Spacecraft and Rockets* **17** (6), 537–545.

W., Mccormack R. 2014 *Numerical Computation of Compressible and Viscous Flow*. American Institute of Aeronautics and Astronautics, Inc.

X., Li S. 2007 *Hypersonic flow characteristics of typical configurations*. National Defense Industry Press.

Y., Wada & S., Liou M. 1994 A flux splitting scheme with high-resolution and robustness for discontinuities. *AIAA Paper* .

Y., You, C., Zhu & J., Guo 2011 Dual waverider concept for the integration of hypersonic inward-turning inlet and airframe forebody. *Aiaa/dlr/dglr International Space Planes & Hypersonic Systems & Technologies Conference* .